Validation of an Extensible Rod Model for Soft Continuum Manipulators

Hunter B. Gilbert, *Member, IEEE,* and Isuru S. Godage, *Member, IEEE*

***Abstract*—Numerous soft and continuum robotic manipulators have demonstrated their potential for compliant operation in highly unstructured environments or near people. Despite their recent popularity, modeling of their smooth bending deformation remains a challenge. For soft continuum manipulators, the widespread, constant curvature approach to modeling is inadequate for modeling some deformations that occur in practice, such as combined bending and twisting deformations. In this paper, we extend the classical Cosserat rod approach to model a variable-length, pneumatic soft continuum arm. We model the deformation of a pneumatically driven soft continuum manipulator, and the model is then compared against experimental data collected from a three degree of freedom, pneumatically actuated, soft continuum manipulator. The model shows good agreement in capturing the overall behavior of the bending deformation, with mean Euclidean error at the tip of the robot of 2.48 cm for a 22 cm long robot. In addition, the model shows good numerical stability for simulating long duration computations.**

I. Introduction

The precursors of continuum robots, such as the hyper-redundant robot of Chirikjian *et al.* [1], brought about new challenges in the kinematic and dynamic modeling of such high-degree-of-freedom structures. The computational power available at the time motivated low-dimensional modeling approaches [2]. As researchers moved from hyper-redundant to continuum structures and began to explore robots made of soft materials, the challenge of modeling them has engendered numerous approaches spanning the full breadth of model complexity, computational complexity, and predictive accuracy.

Soft continuum manipulators, composed of a slender, elastic structure and pneumatically actuated to produce 3D, spatial deformations in both bending and extension (see Fig. 1), bring several modeling challenges to the forefront [3]. The infinite degree-of-freedom deformation of the continuum body poses an immediate difficulty – it is not clear *a priori* what level of model complexity will suffice for a model-based analysis. Ideally, a general-purpose model should produce accurate predictions of the robot shape across a wide variety of actuator input magnitudes and frequencies and should also provide the ability to couple the robot with a dynamic model of its environment.

There are now many models for soft and/or continuously deformable robots. The statics of elastic, rod actuated continuum robots have been modeled via elliptic integrals [4].

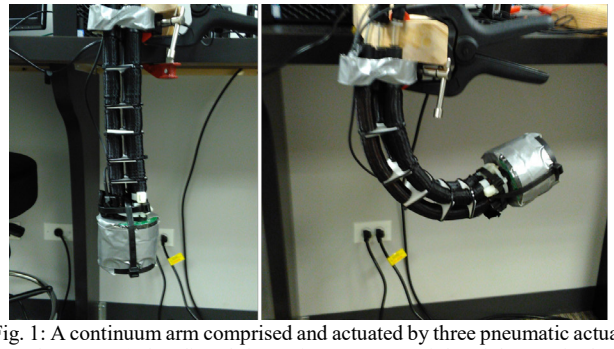

Fig. 1: A continuum arm comprised and actuated by three pneumatic actuator muscles (PAMs). bending deformation. Due to weight of the manipulators, these arms, typically modeled as circular arcs, can deform out of plane.

Dynamic models of a tendon-actuated continuum manipulator have been produced using Kane's method [5]. Lumped-mass models [6], [7] have also been applied to model continuum robot dynamics. Another type of lumped parameter model is the center-of-gravity based model proposed in [8]. However, parameter lumping can require the strong intuition of a good modeler to be successful. The model proposed in [9] employed Lagrangian mechanics to derive planar dynamics for variable-length continuum robots. Utilizing modal methods, the model reported in [10] achieved near real-time performance for variable-length continuum arms, but this model did not include torsional deformations, which may be significant in practical applications.

Cosserat rod theory has been used to model the quasistatic behavior of tendon actuated inextensible flexible backbone [11] and concentric tube continuum robots [12] with kinematic accuracies on the order of a few percent of the length of the structure. Rod models may generally permit bending, twisting, extension, shear, and inflation [13]. These models do not suffer from numerical instabilities inherent in dynamic models based on curve parametric representation of bending deformation. Also, this approach is not limited by the constant curvature assumption, which is overly restrictive in the case of compliant structures, and which results in large discrepancies when out-of-plane deformation occurs under the influence of external forces. Further, Cosserat rod models are sufficiently complex to model twisting deformations of slender arm-like structures, whereas parametric curve models typically assume circular arc deformation to maintain a small set of parameters. Although more computationally intensive to solve than simpler lumped parameter models, Cosserat rod models have been shown to be

H. B. Gilbert is with the Department of Mechanical and Industrial Engineering, Louisiana State University, Baton Rouge, LA 70803, USA.

I. S. Godage is with the School of Computing, DePaul University, DePaul University, Chicago, IL 60604, USA.

This paper is supported in part by the National Science Foundation (NSF) grant no. 1718755. H. G. also thanks the Alexander von Humboldt Foundation for funding that supported this work.

computable at rates of simulation time far exceeding real time for quasistatic cases [14, 15].

The work reported in [16] proposed a Cosserat rod model for a soft manipulator but reported inefficient simulation times of 28 min for 1 s of simulation time; by comparison, our implementation requires about 3 s for 1 s of simulation time. The model in our present work is structurally similar to the model in [16], except that our model for pneumatic actuation is different than the one for cable actuation, and extensibility is a primary concern in our case. Cosserat rod theory has been used to model the dynamics of variable-length continuum arms previously, but the model was validated only for planar, static configurations [17]. Cosserat rod models were also validated for spatial fiber-reinforced pneumatic actuators [18]. Our work extends the Cosserat rod theory with a different actuator coupling than presented in [17]. We also validate the model with three-dimensional, dynamic experimental data to show that it captures the dynamic effects of spatial bending and extension in soft, pneumatic continuum manipulators.

II. Physics-based Model of the Robot

A. Definitions and Assumptions

In what follows, partial derivatives are denoted with comma subscripts. The equations are presented in vectorial form rather than in coordinates. Where applicable, a variable set upright, as in $\mathbf{m}$ contrasted with $\boldsymbol{m}$, refers to the triple of body-frame coordinates $\mathbf{m} = (m_1, m_2, m_3)$, with $m_k = \boldsymbol{m} \cdot \boldsymbol{d}_k$ and with $\boldsymbol{d}_k$ as defined below.

Following Antman [19, Chap. 8], we assume that material points of the three dimensional body are identified by curvilinear coordinates $\boldsymbol{x} = (s, x^1, x^2)$ and a time variable t such that

$$\boldsymbol{p}(\boldsymbol{x}, t) = \boldsymbol{r}(s,t) + x^1 \boldsymbol{d}_1(s,t) + x^2 \boldsymbol{d}_2(s,t)\,, \qquad (1)$$

where $\boldsymbol{p}(\boldsymbol{x}, t)$ is the position vector of a material point in an inertial reference frame. The curve $\boldsymbol{r}$ is referred to as the axis or centerline and $\boldsymbol{d}_1(s,t)$ and $\boldsymbol{d}_2(s,t)$ are termed the director vectors. The coordinates x^1 and x^2 locate a material point in a cross-section perpendicular to the centerline $\boldsymbol{r}(s,t)$.

The robot shape is described entirely by the rod configuration $C(t)$, defined as

$$\boldsymbol{C}(t) = \{\boldsymbol{r}(s,t), \boldsymbol{d}_1(s,t), \boldsymbol{d}_2(s,t)\}. \qquad (2)$$

The special configuration $C^0 = \{\boldsymbol{r}^0(s), \boldsymbol{d}_1^0(s), \boldsymbol{d}_2^0(s)\}$ is termed the reference configuration of the rod, which is assumed to be known. The coordinate s must generally only satisfy the property that $|\boldsymbol{r}_{,s}| > 0$, but we assume that s measures arc length in the reference configuration, i.e. $|\boldsymbol{r}^0{}_{,s}| = 1$. In all cases it is assumed that $\boldsymbol{r}(s,t)$ describes the neutral axis of bending, and that by symmetry of the mass distribution the first moment of mass in a cross section taken perpendicular the centerline also vanishes.

B. Differential Geometric Description

The director vectors, when augmented by the third director $\boldsymbol{d}_3(s,t) = \boldsymbol{d}_1(s,t) \times \boldsymbol{d}_2(s,t)$, form an orthonormal basis for three-dimensional space, and therefore their derivatives with respect to s and with respect to t must satisfy relations of the forms

$$\begin{aligned} \boldsymbol{d}_{k,s}(s,t) &= \boldsymbol{u}(s,t) \times \boldsymbol{d}_k(s,t) \\ \boldsymbol{d}_{k,t}(s,t) &= \boldsymbol{\omega}(s,t) \times \boldsymbol{d}_k(s,t)\,. \end{aligned} \qquad (3)$$

These equations define $\boldsymbol{u}(s,t)$ and $\boldsymbol{\omega}(s,t)$. The functions $\boldsymbol{u}$ and $\boldsymbol{\omega}$ automatically satisfy an equation of constraint

$$\boldsymbol{u}_{,t} = \boldsymbol{\omega}_{,s} - \boldsymbol{u} \times \boldsymbol{\omega}\,. \qquad (4)$$

The vector $\boldsymbol{u}$ represents flexure, while the vector $\boldsymbol{\omega}$ represents angular velocity.

The position vector $\boldsymbol{r}(s,t)$ satisfies the differential relationships

$$\begin{aligned} \boldsymbol{r}_{,s}(s,t) &= \boldsymbol{v}(s,t) \\ \boldsymbol{r}_{,t}(s,t) &= \boldsymbol{\eta}(s,t)\,. \end{aligned} \qquad (5)$$

These two equations define $\boldsymbol{v}$ and $\boldsymbol{\eta}$. The variable $\boldsymbol{v}(s,t)$ is a strain variable measuring shear and extension, and the variable $\boldsymbol{\eta}$ is the velocity of the point at $\boldsymbol{r}(s,t)$. At any given time, the variables $\boldsymbol{u}(s,t)$ and $\boldsymbol{v}(s,t)$, together with boundary conditions, possess enough information to determine the configuration $C(t)$. As with the constraint on $\boldsymbol{u}$ and $\boldsymbol{\omega}$, there is likewise a constraint on $\boldsymbol{v}$ and $\boldsymbol{\eta}$, which simply states that the mixed partial derivatives are equal:

$$\boldsymbol{v}_{,t} = \boldsymbol{\eta}_{,s}\,. \qquad (6)$$

C. Equations of Dynamic Equilibrium

The following classical special Cosserat equations are the equations of motion [19, p. 278]. The arguments s and t have been suppressed for conciseness.

$$\begin{aligned} (\rho A)\boldsymbol{\eta}_{,t} &= \boldsymbol{n}_{,s} \\ (\rho \boldsymbol{J} \cdot \boldsymbol{\omega})_{,t} &= \boldsymbol{m}_{,s} + \boldsymbol{r}_{,s} \times \boldsymbol{n} \end{aligned} \qquad (7)$$

In these equations, $\boldsymbol{n}(s,t)$ represents the internal force and $\boldsymbol{m}(s,t)$ represents the internal moment. The quantity (ρA) is the mass density per unit reference length, which is assumed to be uniform, and $(\rho \boldsymbol{J})$ is the positive definite second mass moment of inertia (per unit length) of the axial cross section, which is also assumed to be uniform. It is natural to allow the angular momentum per unit length $(\rho \boldsymbol{J} \cdot \boldsymbol{\omega})$ and the linear momentum per unit length $(\rho A)\boldsymbol{\eta}$ to be state variables.

D. Constitutive Material Behavior

The response of the robot structure to deformation is modeled by a single lumped-parameter viscoelastic constitutive behavior, modeled after the Kelvin-Voigt constitutive law. The laws are specified in the body-frame coordinates to ensure invariance of the material behavior under rigid body transformations.

$$\begin{aligned} \boldsymbol{m}(s,t) &= \boldsymbol{K}_b\big(\boldsymbol{u}(s,t) - \boldsymbol{u}_F(s,t)\big) + \boldsymbol{B}_b \boldsymbol{u}_{,t}(s,t) \\ \boldsymbol{n}(s,t) &= \boldsymbol{K}_e\big(\boldsymbol{v}(s,t) - \boldsymbol{v}_F(s,t)\big) + \boldsymbol{B}_e \boldsymbol{v}_{,t}(s,t) \end{aligned} \qquad (8)$$

The matrix $\boldsymbol{K}_b$ represents the stiffness in flexure, $\boldsymbol{B}_b$ the flexural damping, $\boldsymbol{K}_e$ the stiffness in shear and extension, and $\boldsymbol{B}_e$ the damping in shear and extension. The variables $\boldsymbol{u}_F(s,t)$ and $\boldsymbol{v}_F(s,t)$ are the stress-free values of the strain variables. When no actuation is present, these are equal to $\boldsymbol{u}^0(s)$ and $\boldsymbol{v}^0(s)$. We assume in all simulations that follow that these four matrices are diagonal and positive.

As an approximation to the robot's structure, we presently assume that the constitutive parameters are those of a cross section composed of three thick-walled cylinders, positioned at equal angular spacing with radial symmetry. Thus, in body-frame coordinates, these matrices take the following forms:

$$\boldsymbol{K}_b = \mathrm{diag}(EI, EI, GJ)$$
$$\boldsymbol{K}_e = \mathrm{diag}(EA, EA, GA)$$

where E and G are the Young's modulus and shear modulus, A is the effective cross-sectional area, I is the effective second moment of area about either the $\boldsymbol{d}_1$- or $\boldsymbol{d}_2$-axis, and J is the effective polar second moment of area. The parameters $\boldsymbol{B}_b$ and $\boldsymbol{B}_e$ are chosen as scalar multiples of $\boldsymbol{K}_b$ and $\boldsymbol{K}_e$, respectively.

E. Boundary Conditions

The robot is subject to boundary conditions on the unknown variables that model the physical scenario. The following boundary conditions apply for the experiment described in the following section.

$$\begin{aligned} \boldsymbol{m}(L,t) &= \boldsymbol{m}_1(t) \\ \boldsymbol{n}(L,t) &= \boldsymbol{n}_1(t) \\ \boldsymbol{r}(0,t) &= \boldsymbol{0} \\ \boldsymbol{d_1}(0,t) &= \hat{\boldsymbol{\imath}} \\ \boldsymbol{d_2}(0,t) &= \hat{\boldsymbol{\jmath}} \end{aligned} \tag{9}$$

The boundary condition functions $\boldsymbol{m}_1(t)$ and $\boldsymbol{n}_1(t)$ represent the interaction of the robot with its environment through a moment and force. The unit vectors $\hat{\boldsymbol{\imath}}$ and $\hat{\boldsymbol{\jmath}}$ represent the first two coordinate axes of the lab coordinate frame.

F. Initial Conditions

In the simulations that follow, we assume the initial conditions

$$\begin{aligned} (\rho \boldsymbol{J} \cdot \boldsymbol{\omega})(s,0) &= \boldsymbol{0} \\ (\rho A)\boldsymbol{\eta}(s,0) &= \boldsymbol{0} \\ \boldsymbol{u}(s,0) &= \boldsymbol{u}^0(s) \\ \boldsymbol{v}(s,0) &= \boldsymbol{v}^0(s) \end{aligned} \tag{10}$$

These conditions model the robot initially at rest in the unactuated and undeformed state.

G. Pneumatic Actuation

The pneumatic actuators cause internal stresses in the structure of the robot. They can be included without any additional changes to the model as a change in the stress-free values of the strain variables $\boldsymbol{u}_F(s,t)$ and $\boldsymbol{v}_F(s,t)$, such that each actuator tends to produce constant-curvature bending whenever they are pressurized. Assume that when an actuator is pressurized, it produces an internal force component which is normal to the axial cross section according to the linear model $n_i = P_i A_{\text{eff}}$, where A_{eff} is the effective area of the actuator and p_i is the air pressure in the chamber of the ith actuator. Then, the net internal actuator force and moment are

$$\begin{aligned} \boldsymbol{m}_{\text{act}}(t) &= A_{\text{eff}} \sum_i P_i \boldsymbol{z}_i \\ \boldsymbol{n}_{\text{act}}(t) &= A_{\text{eff}} \sum_i P_i \boldsymbol{d}_3 \end{aligned} \tag{11}$$

The vectors $\boldsymbol{z}_i$ are equal to the cross product of the coordinates of the center of the actuator in the material cross section and $\boldsymbol{d}_3$, the direction of the induced force due to pressurization of that actuator (always, the third standard basis vector, in the material coordinate frame).

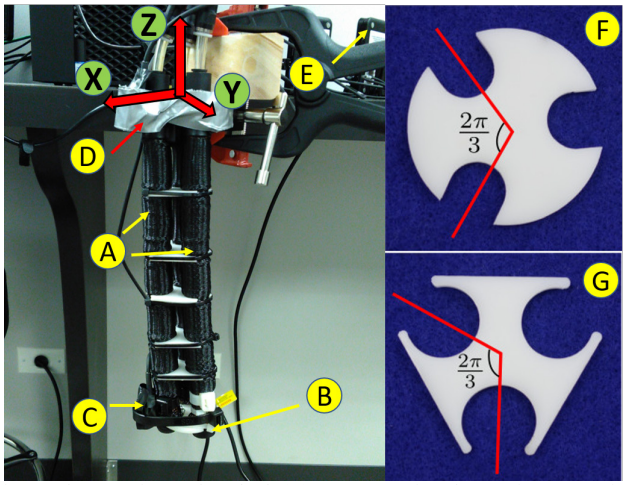

Fig. 2: The experimental testbed, (A) PAS powering the continuum section, (B) external load rigidly attached at the tip of the robot, (C) & (E) magnetic tracker attached to the side of the arm to measure the tip and base respectively, (D) Polhemus G4 wireless position tracking hub, (F) PAM mounting plates that are used in the base and the tip, and (G) constraining plats installed along the continuum robot to ensure PAM deformation in parallel to the neutral axis of the robot.

The stress-free values of the strain variables are then given by the following equations,

$$\begin{aligned} \mathbf{u}_F(s,t) &= \mathbf{u}^0(s) + \boldsymbol{K}_b^{-1}\mathbf{m}_{\text{act}} \\ \mathbf{v}_F(s,t) &= \mathbf{v}^0(s) + \boldsymbol{K}_e^{-1}\mathbf{n}_{\text{act}} \end{aligned} \tag{12}$$

in which $\mathbf{u}^0(s)$ and $\mathbf{v}^0(s)$ are the curvature and linear strain variables for the reference (original stress-free) configuration. Note that the boundary conditions on $\boldsymbol{m}$ and $\boldsymbol{n}$ must still apply in place of the constitutive laws at the distal end of the manipulator. The equations (7), (8), and (12) imply that at static equilibrium and under free boundary conditions $\boldsymbol{m}_1 = 0$ and $\boldsymbol{n}_1 = 0$, the curvature $\mathbf{u} = \mathbf{u}^0 + \boldsymbol{K}_b^{-1}\mathbf{m}_{\text{act}}$.

In general, the A_{eff} may be calibrated values for each actuator. However, one must take care that these parameters cannot be simultaneously calibrated with the inertia parameters ρA and $\rho \boldsymbol{J}$, the stiffness parameters $\boldsymbol{K}_\alpha$, and the damping parameters $\boldsymbol{B}_\alpha$, since this would result in a gauge freedom in the set of calibration parameters.

III. Materials and Methods

A. Experimental Testbed

The prototype continuum section shown in Fig. 2 consists of three mechanically identical extending pneumatic actuator muscles (PAMs) with an unactuated length of 0.22 m and a maximum extension of 0.071 m at 4 bars. Silicone rubber tubes of inner diameter (ID) 10mm and outer diameter (OD) 13mm were used as the PAM bladders. Nylon union tube connectors (ID=6mm) were utilized to mount the Silicone tubes at each end because of the low cost and ease of use. The pressure-supplying plastic tubes are directly pluggable to union connectors of one end of PAM and the other is closed with a Nylon blanking plug. The Polyester braided sheath (minimum OD = 13 mm, maximum OD = 25 mm) is then inserted and tightened with high strength Nylon cable ties.

Rigid plastic mount frames of 0.0175 m radius and 2.54 mm thickness are used to mount the PAMs. Rigid plastic constrainers (Fig. 2-G) help constrain PAM's to operate parallel to the neutral axis at designated clearance ($2\pi/3$ rad apart) from each other as well as provide improved torsional stiffness.

Each continuum section, inclusive of the tubing and constrainers has an approximate mass of 0.165kg. The pressure to each PAM of the continuum arm section is controlled by one of three PNEUMAX 171E2N.T.D.0009S digital proportional pressure regulators, which are controlled by analog signals generated by a NI PCI-6289 DAQ card with the MATLAB Desktop Realtime testing environment. Due to the gradual pressure buildup in PAMs the maximum pressure increase rate is upper-bounded at about 3 kPa/s.

A Polhemus G4 wireless magnetic tracking system (Fig. 2-D) is used to obtain the continuum section deformation in space. Two 6 DoF trackers were rigidly attached to the side of the base and the end-effector of the continuum section (see Fig. 2-C & E). Rigid body transformation techniques are then used to find the tip and base positions in data post processing. The internal pressure of PAMs and the task-space position and orientation were recorded at 50 Hz for the duration of each experiment.

B. Experimental System Excitation

To validate the dynamic model, a set of alternating square pulses was applied independently to each actuator for a duration of 5 seconds. The square pressure pulses are applied such that the system undergoes repeated step responses along different spatial directions. The 5 s time window was chosen to ensure that both transient and steady-state phenomena were captured. The input functions are depicted graphically in Fig. 3. Prior to the beginning of each experiment, the robot was at rest under zero pressure.

C. Model Implementation

For computation, the equations of § II are implemented in spatial coordinates. Explicitly, as shown in [20], the eighteenth-order system of quasilinear equations is

$$\begin{aligned} \boldsymbol{d}_{k,t} &= \boldsymbol{\omega} \times \boldsymbol{d}_k \ , \ \ k = 1,2 \\ \boldsymbol{v}_{,t} &= \boldsymbol{\eta}_{,s} \\ \boldsymbol{u}_{,t} &= \boldsymbol{\omega}_{,s} - \boldsymbol{u} \times \boldsymbol{\omega} \\ \rho A \boldsymbol{\eta}_{,t} &= \boldsymbol{n}_{,s} \\ (\rho \boldsymbol{J} \cdot \boldsymbol{\omega})_{,t} &= \boldsymbol{m}_{,s} + \boldsymbol{v} \times \boldsymbol{n} \end{aligned} \tag{13}$$

The set of equations is closed by the constitutive laws in (8). In order to evaluate the laws, note that $\boldsymbol{v}_{,t}$ and $\boldsymbol{u}_{,t}$ are first evaluated and then transformed to the local coordinate frame. The value of $\boldsymbol{u}^0(s)$ was assumed to be zero and the value of $\boldsymbol{v}^0$ was taken to be the standard choice $\mathbf{v}^0 = (0,0,1)$.

For numerical integration of the equations, the method of lines was implemented using MATLAB's *ode23t* ordinary differential equation solver, which uses the implicit trapezoidal rule. Spatial derivatives were approximated by the standard, second-order-accurate central finite difference scheme on an equally spaced grid with 10 points.

Note that the position $\boldsymbol{r}$ is not required for the solution of the model when no external environmental interaction is present. Our implementation first solves the set of equations (13) and then reconstructs the shape by solving (5) numerically using the exponential Euler integrator

$$T(s_{i+1}) = T_i \exp\left(h\hat{\xi}(s_i, t)\right)$$

where exp is the matrix exponential, $\hat{\xi}$ is the element of $\mathfrak{se}(3)$ defined by the body-frame coordinates $\mathbf{u}$ and $\mathbf{v}$, and h is the distance between the nodes in the finite difference method.

D. Model Parameter Calibration

Parameter calibration was performed manually by visual inspection and iterative computation of the sum squared error between the measured and modeled positions of the manipulator end effector. Only two of the model parameters were optimized: the scalar parameter τ relating $\boldsymbol{B}_b = \tau \boldsymbol{K}_b$ and $\boldsymbol{K}_e = \tau \boldsymbol{K}_b$ [21], and the effective area A_{eff} of the PAM actuators (i.e. the pressure-to-force relationship). The remaining two actuators are assumed to have the same properties as the first, and to be perfectly located according to the design. An additional coordinate registration was calibrated by rotation about the base z-axis (along the long axis of the robot) and translation along the base x- and y- axes. The mass parameters ρA and $\rho \boldsymbol{J}$ are not calibrated to avoid a gauge freedom. These parameters are instead calculated based on the measured mass of the robot and the physical dimensions of the design.

IV. Results and Discussion

A. Validation without external loads

Fig. 3 displays the calibrated model simulation against the experimental data for the square-wave based pressure inputs. The calibrated final parameter values were $\tau = 0.19\ s$, and $A_{\text{eff}} = 1.45 A_{\text{nom}}$ where $A_{\text{nom}} = \pi D^2/4$ for $D = 10$ mm.

The overall tip error ranges from 0 to approximately 0.1 m. The absolute error in the end-effector location reaches a maximum of 20 cm at 91 s, although we note that this is a suspected measurement outlier. The next largest error is 11.2 cm, occurring at 115 s during a high-pressure actuation of 3.6 bar. The mean absolute error at the end effector over the entire time frame was 2.48 cm. Note that this mean error does include the time windows in which the pressure returns to the resting low-pressure state.

The model solution exhibits some underdamped behavior, with slight oscillation in some coordinate values for many of the square pressure inputs. The experimental data, however, does not exhibit oscillation or overshoot for most of the step inputs. Rise times in the experimental data are approximately between 150 ms and 300 ms, with the corresponding model rise times being slightly slower, from approximately 300 to 400 ms. When τ is tuned to remove all oscillation from the model, the discrepancy in rise time increases.

Fig. 4 b-f shows snapshots of the visualization of the simulation results corresponding to Fig. 3. Fig. 4 a-b shows a simulation for the case of pure extension. Due to the constrained arrangement, when pressure is applied to all the actuators simultaneously, it causes the arm to extend without bending. This behavior is poorly modeled in the standard curve parametric models due to ill-conditioning of mathematical expressions. Yet, the proposed model captures this behavior

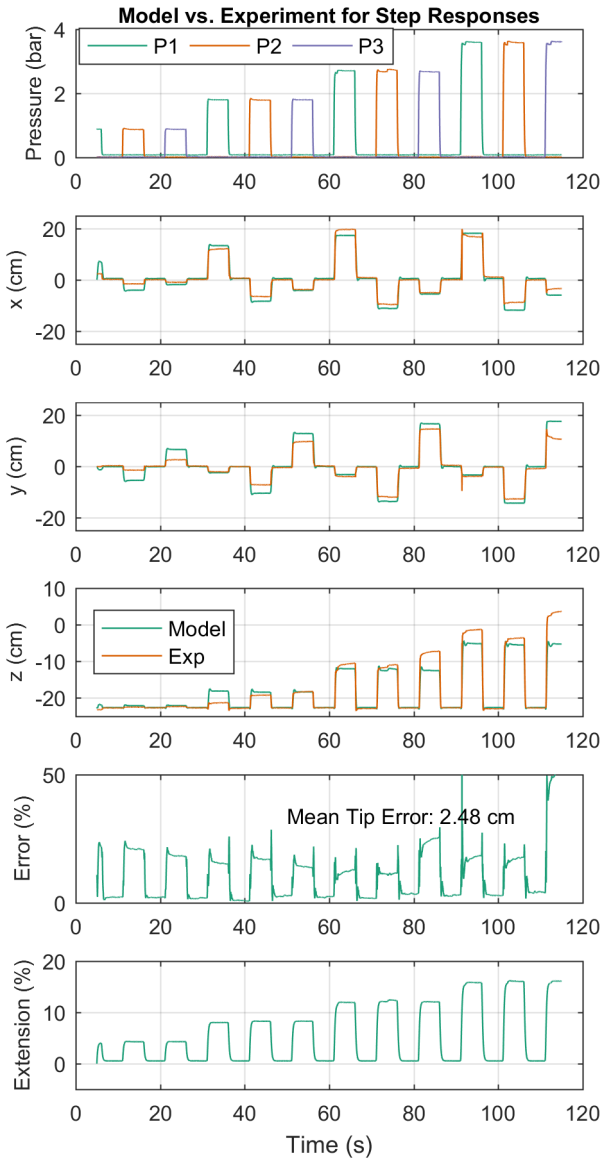

Fig. 3. Comparison of model and experimental data for square pressure inputs of varying magnitudes. The pressure inputs closely match the desired pattern of square pulses.

without any problems. In addition, the readers are referred to the accompanying video to observe the complete simulation.

B. Discussion

The model predictions are generally in good qualitative agreement with the experimental results. The deflections represented in the experimental data are large relative to the length of the robot, and at the highest input pressures, the z-coordinate of the end-effector location reaches nearly to the x-y plane where the base of the robot is located. In Fig. 3, the square shape of the input pressure pulses is clearly reflected in the position output at the end-effector both in the experimental data and in the model data. Similar qualitative agreement is observed for the triangular pressure inputs.

The extension shown in Fig. 3 is an important feature of this model. Extensions up to approximately 16% were simulated by the model during the step input sequence. A simultaneous pressure of 4 bar applied to all three actuators

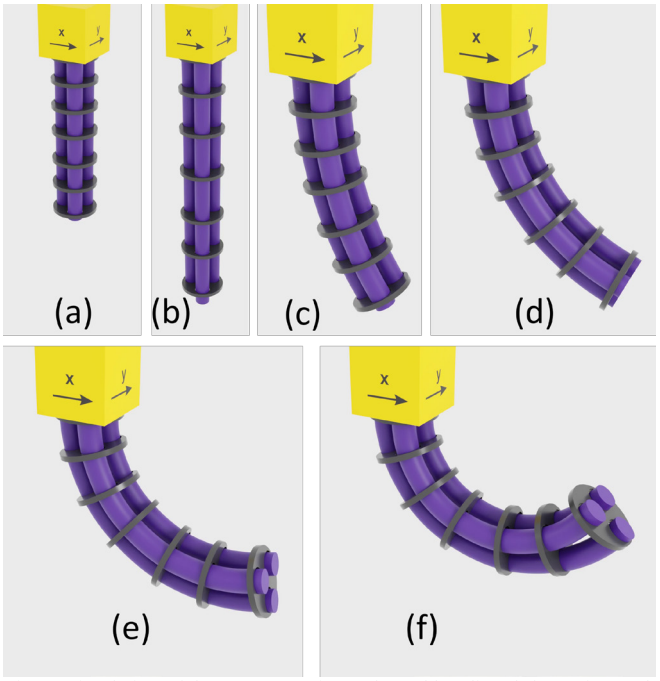

Fig. 4: Simulation of the pure extension (a-b) and bending deformation (c-f) of the proposed variable-length rod model.

produces a modeled extension of 52% of the original length of the robot. We note that this is an overprediction, since the actuators produce an extension of 32% of their length under the same conditions. This discrepancy is likely due to the unmodeled nonlinearity of the force-displacement relationship for pneumatic muscle actuators [22]. Regardless, these large changes in length are important not only to the kinematics but also to the dynamic behavior, which is automatically captured by the Cosserat rod-based model. Although the assumptions of shear-free and extension-free deformation are common for the modeling of rods made of stiffer materials, such assumptions for this robot would be disastrous. In typical cases, the assumptions are made because the differential equations become too stiff, preventing efficient numerical simulation. Because of the relatively soft elastomeric material, no such difficulty is encountered in this application.

There exists a clearly observed pattern in the Euclidean tip position error, which correlates with the application of high input pressures. This correlation likely indicates both the presence of unmodeled physical effects and an incomplete model calibration. We therefore strongly believe that the level of accuracy may be improved by the inclusion of further physical effects into the model, and/or through calibration of additional model parameters via optimization.

The material constitutive laws were chosen as a convenient and common first approach. Because of the composite structure, it is reasonable to assume that one may find different constitutive laws that provide a more accurate prediction of the behavior. The over-prediction of the displacement for low pressures is consistent with the presence of significant amounts of coulomb-type friction, but other sources of error may include material hysteresis, and nonlinear material response. At higher pressure inputs, the model faithfully reproduces the experimentally observed behavior in a qualitative sense, with absolute accuracy not substantially

different than the accuracy for low-pressure inputs. Because the model both under- and over-predicts displacements with equal frequency, further model parameter fitting is unlikely to resolve the majority of the remaining error.

Manufacturing errors, differences between the three actuators' ability to transform pressure into force, and measurement errors may also be responsible for some of the observed misfit between the experimental data and the model. Note that the model predictions were not used to register the two coordinate systems except in the case of the hand-tuned rotation about the base z-axis. For these reasons, we believe that increasing the number of free model parameters (for instance, allowing each actuator to have its own effective area) may improve the model accuracy.

The number of fitted model parameters was kept to a minimum at present because the current implementation of the model in Matlab requires approximately 3.3 s to simulate 1 s of model time on a Xeon E3-1245v5 CPU, and therefore the computational burden of parameter optimization is currently high for a desktop workstation. We expect, based on our own prior experience and on the recent work on concentric tube robots by Leibrandt *et al.* [15], that the model's performance can be greatly accelerated by implementation in a compiled language. The finite-difference method, which was used to implement the method of lines, may also be accelerated by parallel computation on hardware accelerators.

Lastly, we note that the numerical integrator chosen, Matlab's *ode23t*, possesses no numerical damping. This choice is only feasible due to the material constitutive law that explicitly includes physical damping effects. As a result, numerical damping is not required to maintain numerical stability. The model demonstrates good long-term stability, and in these tests the model showed no signs of numerical instability within the 116 s simulation. The simulation of a robot with a much longer length of 1 m, but with all other properties remaining the same, also showed no signs of instability. Using a physical source of damping and an integrator without numerical damping permits models of the physics to be explored with less concern for changes in step size or spatial discretization.

V. Conclusion

Cosserat rod theory has been successfully applied to generate many kinematic and dynamic models in the continuum robotics community to date, and with this work we have demonstrated its applicability as a tool for building dynamic models of pneumatic soft continuum manipulators. The single Cosserat rod model was able to accurately reproduce the experimental observations of a pneumatic continuum manipulator quantitatively and qualitatively. However, room for improvement does remain. In particular, the incorporation of more complex material and actuator models, a more thorough exploration of the parameter space, and an accelerated implementation of the model will be particular areas of focus in future work. Additionally, coupling the robot to environmental loads remains to be validated experimentally. Nevertheless, we believe that the Cosserat rod-based model displays great promise for making accurate dynamic predictions of soft continuum manipulators.

References

[1] G. S. Chirikjian and J. W. Burdick, "Design and Experiments with a 30 DOF Robot," in *IEEE International Conference on Robotics and Automation*, 1993, pp. 113-119.

[2] G. S. Chirikjian and J. W. Burdick, "A modal approach to hyper-redundant manipulator kinematics," *IEEE Transactions on Robotics and Automation,* vol. 10, no. 3, pp. 343-354, 1994.

[3] K. Suzumori, S. Iikura, and H. Tanaka, "Development of flexible microactuator and its applications to robotic mechanisms," in *IEEE International Conference on Robotics and Automation*, 1991, pp. 1622-1627.

[4] K. Xu and N. Simaan, "Analytic Formulation for Kinematics, Statics, and Shape Restoration of Multibackbone Continuum Robots Via Elliptic Integrals," *Journal of Mechanisms and Robotics,* vol. 2, no. 1, p. 011006, 2010.

[5] W. S. Rone and P. Ben-Tzvi, "Continuum robot dynamics utilizing the principle of virtual power," *IEEE Transactions on Robotics,* vol. 30, no. 1, pp. 275-287, 2014.

[6] N. Giri, "A New Approach to Dynamic Modeling of Continuum Robots," Clemson University, 2011.

[7] T. Mahl, A. E. Mayer, A. Hildebrandt, and O. Sawodny, "A Variable Curvature Modeling Approach for Kinematic Control of Continuum Manipulators," in *American Control Conference*, 2013, pp. 4945-4950.

[8] I. S. Godage, R. Wirz, I. D. Walker, and R. J. Webster, "Accurate and Efficient Dynamics for Variable-Length Continuum Arms: A Center of Gravity Approach," *Soft Robotics,* vol. 2, no. 3, pp. 96-106, 2015.

[9] A. D. Kapadia, I. D. Walker, D. M. Dawson, and E. Tatlicioglu, "A New Approach to Extensible Continuum Robot Control Using the Sliding-Mode," *Computer Technology and Application,* vol. 2, no. 4, pp. 293-300, 2011.

[10] I. S. Godage, G. A. Medrano-Cerda, D. T. Branson, E. Guglielmino, and D. G. Caldwell, "Dynamics for variable length multisection continuum arms," *The International Journal of Robotics Research,* vol. 35, no. 6, pp. 695-722, 2016.

[11] B. A. Jones, R. L. Gray, K. Turlapati, and S. Member, "Three Dimensional Statics for Continuum Robotics," in *IEEE/RSJ International Conference on Intelligent Robots and Systems*, 2009, pp. 2659-2664.

[12] D. C. Rucker, B. A. Jones, and R. J. Webster, "A geometrically exact model for externally loaded concentric-tube continuum robots," *IEEE Transactions on Robotics,* vol. 26, no. 5, pp. 769-780, 2010.

[13] I. Tunay, "Spatial continuum models of rods undergoing large deformation and inflation," *IEEE Transactions on Robotics,* vol. 29, no. 2, pp. 297-307, 2013.

[14] H. B. Gilbert, D. C. Rucker, and R. J. Webster, "Concentric tube robots: The state of the art and future directions," in *Robotics Research*, vol. 114, 2016, pp. 253-269.

[15] K. Leibrandt, C. Bergeles, and G. Yang, "Concentric Tube Robots: Rapid, Stable Path-Planning and Guidance for Surgical Use," *IEEE Robotics & Automation Magazine,* vol. 24, no. 2, pp. 42-53, 2017.

[16] F. Renda, M. Giorelli, M. Calisti, M. Cianchetti, and C. Laschi, "Dynamic model of a multibending soft robot arm driven by cables," *IEEE Transactions on Robotics,* vol. 30, no. 5, pp. 1109-1122, 2014.

[17] D. Trivedi, A. Lotfi, and C. D. Rahn, "Geometrically exact dynamic models for soft robotic manipulators," *IEEE Transactions on Robotics,* vol. 24, pp. 1497-1502, 2008.

[18] N. K. Uppalapati and G. Krishnan, "Towards Pneumatic Spiral Grippers: Modeling and Design Considerations," *Soft robotics,* vol. 5, no. 6, pp. 695-709, 2018.

[19] S. S. Antman, *Nonlinear Problems of Elasticity* (Applied Mathematical Sciences, no. 107). New York: Springer-Verlag, 2005.

[20] S. S. Antman and T. I. Seidman, "The Parabolic-Hyperbolic System Governing the Spatial Motion of Nonlinearly Viscoelastic Rods," *Archive for Rational Mechanics and Analysis,* vol. 175, no. 1, pp. 85-150, 2005.

[21] J. Linn, H. Lang, and A. Tuganov, "Geometrically exact Cosserat rods with Kelvin–Voigt type viscous damping," *Mech. Sci.,* vol. 4, no. 1, pp. 79-96, 2013.

[22] W. Liu and C. Rahn, "Fiber-reinforced membrane models of McKibben actuators," *Journal of Applied Mechanics,* vol. 70, no. 6, pp. 853-859, 2003.